

Muonium reaction in MgO: A showcase for the final steps of ion implantation

Rui C. Vilão^{1*}, Ali Roonkiani¹, Apostolos G. Marinopoulos¹, Helena V. Alberto¹, João M. Gil¹, Ricardo B. L. Vieira¹, Robert Scheuermann² and Alois Weidinger³

¹ University of Coimbra, CFisUC, Department of Physics,
P-3004-516 Coimbra, Portugal

² Laboratory for Muon-Spin Spectroscopy, Paul Scherrer Institut,
5232 Villigen PSI, Switzerland

³ Helmholtz-Zentrum Berlin für Materialien und Energie, Department ASPIN,
14109 Berlin, Germany

* ruivilao@uc.pt

Abstract

We present an in-depth investigation of the implantation of positive muons in magnesium oxide (MgO). Muonium, the positive muon plus an electron is an analogue of the hydrogen atom. This study describes the final stage of the implantation process, from muon diffusion over the potential barrier and the stopping by an inelastic reaction to the final embedding of the muon into the lattice structure. A special aspect is a relatively long-lived intermediate configuration which lasts for several hundred nanoseconds or more and is accessible to muon spin spectroscopy. The model presented here provides a framework for the analysis of the general case of ion implantation.

Copyright attribution to authors.

This work is a submission to SciPost Physics.

License information to appear upon publication.

Publication information to appear upon publication.

Received Date

Accepted Date

Published Date

1

2 Contents

3	1 Introduction	2
4	2 Experimental Results	3
5	3 Theory	8
6	3.1 Ab-initio (DFT) calculations	8
7	3.2 Muonium configurations in MgO	8
8	3.3 Diffusion barrier for muonium migration	9
9	3.4 The doorway model	10
10	4 Discussion	12
11	4.1 Formation and decay of the doorway state	12
12	4.2 Properties of the long-lived doorway state	15
13	5 Conclusions	17

14	A Methods	18
15	A.1 Experimental details and methods	18
16	A.1.1 Correction for time resolution.	19
17	A.2 DFT calculations: Setup and preliminaries	19
18	References	20
19	<hr/>	
20		

21 1 Introduction

22 The stopping process of ions in solids is a topic of great importance for a wide range of scientific
23 and technological subjects, including nuclear industry [1], high-energy density physics [2],
24 inertial confinement fusion [3], hadron-therapy in medicine [4], photovoltaic technology for
25 space applications [5], microelectronics [6], or in ion beam technologies [7]. Although the
26 stopping process is rather well understood for the high-energy region, very little is known
27 about the final thermalization process [8–12]. A particularly important case is the stopping
28 of protons in matter. Despite its importance, the proton stopping process, particularly at the
29 low-energy limit, remains challenging and poorly understood [13–16].

30 In this work we investigate the final steps in the implantation of positive muons in the
31 dielectric oxide MgO, using muon spin spectroscopy (μ SR). μ SR is an established experimental
32 method in materials research [17, 18]. Despite their leptonic nature, positive muons can be
33 considered in condensed-matter physics as light pseudo-isotopes of hydrogen, being only c. 9
34 times lighter than the proton. These particles can therefore be used to model the behaviour
35 of protons in condensed-matter systems, also allowing to extend towards isotopic studies of
36 hydrogen in the high-dilution limit, which is typically hard to investigate [19–21]. The use
37 of μ SR lies in the implantation of positive muons in solids with a high kinetic energy of 4
38 MeV (although muons moderated to keV energies are sometimes used as well [22]) and on
39 the experimental observation of the final stable configurations, from which information about
40 hydrogen is extracted.

41 The stopping process of the 4 MeV muons is typically very fast and is not easily accessible
42 experimentally in the time-window of the μ SR experiments. The details of the thermalization
43 process are nevertheless crucial for a correct assessment of the final observed muonium con-
44 figurations and their translation for the physics of hydrogen in semiconductors [23, 24]. The
45 energy dissipation process begins with the well-known Bethe-Bloch mechanism, followed by
46 a fast charge-exchange regime which ends up when the kinetic energy of the muon is lower
47 than the lowest available electronic excitation (1 to a few eV, the typical order of magnitude
48 of the bandgap energy in semiconductors and insulators) [25, 26]. The mechanism for the
49 dissipation of the remainder of the implanted ion kinetic energy to thermal energies remains
50 however largely unknown [25–28]. As is well known for long, phonons play a crucial role in
51 the trapping of the muon/proton in its final stopping site [29].

52 Usually, information on the embedding process of the muon in the lattice is drawn indi-
53 rectly from the stable configurations finally observed in the experiment. In semiconductors
54 and insulators and below room temperature, these reactions occur frequently on a time scale
55 of nanoseconds to microseconds and thus fall within the time window of μ SR [26, 30, 31]. In
56 these cases, the μ SR method offers a unique possibility to explicitly observe also the interme-
57 diate steps before the muon is finally incorporated in the lattice.

58 This possibility offered by μ SR allowed to unveil details of these last stages. In particular, in
59 past experiments in oxides it was shown that a fast-relaxing muon component corresponded

60 to a transient configuration with a fluctuating and very small electronic spin density at the
61 muon [31]. A barrier model has been developed for the branching from this "transition-state"
62 to the final configurations (oxygen-bound and interstitial muonium) [32]. We have also iden-
63 tified a thermal spike effect due to the energy liberated during the muon stopping process and
64 the stress release by the relaxation of the lattice [33], akin to the long known thermal spike
65 effect thoroughly described in the ion implantation literature [34–36]. This model was sub-
66 sequently and successfully applied to several oxide and semiconducting systems [37–40]. A
67 critical discussion of this model, with a thorough review of previous literature, can be found
68 in Refs. 24, 27 and 28.

69 In this work we aim at further developing the previous model by elucidating the mechanism
70 by which muonium is finally incorporated into the host lattice. We develop and present a
71 model whose basic assumption is that muonium is eventually stopped by a strong inelastic
72 process leading to a temporary muonium configuration which subsequently decays into the
73 final configurations. Because of the central role of this inelastic process, which stands at the
74 beginning of the whole reaction, we use the names "doorway model" and "doorway state" for
75 the corresponding model and state. It indicates that the further course of the reaction is via
76 this entrance configuration.

77 In order to develop and present this doorway model, we use magnesium oxide (MgO) as
78 a benchmark solid and put forward experimental evidence on this last stage of thermaliza-
79 tion. The interest in the investigation of the muonium states in MgO arose from the success
80 of muonium studies in the clarification of the behaviour of the hydrogen impurity in semi-
81 conductors and insulators [19–21]. Magnesium oxide is a rather versatile material currently
82 being used or in consideration for applications in magnetic tunnel junction, catalysis, photo-
83 voltaics or photonics [41–45]. The attraction of hydrogen to the MgO surface and its influence
84 on hydrogen migration has been studied [42, 46]. The investigation of hydrogen in MgO has
85 few limited studies in the past, due to the usual difficulty in investigating hydrogen impurity
86 directly [42, 47, 48], although hydrogen treatments are usually performed in contemporary
87 device building [49].

88 Some μ SR experiments on MgO have been carried out in the past [20, 23]: atomic-like
89 muonium has been reported both at 6 K and at room temperature with significant change in
90 its relaxation rate [50–52]. The corresponding reduced hyperfine parameter at 300 K was
91 reported to be 0.86246(6), corresponding to 3849.4(3) MHz [53]. β -NMR experiments in
92 MgO also revealed a frequency shift of 100 ppm that the authors consider to be likely from a
93 significant transient population of carriers related to the implantation itself [54].

94 The present paper is therefore centered in the presentation and development of the door-
95 way model, taking these novel data on MgO as a particularly illuminating example. The paper
96 is organized in the following way: in the next section (section 2) we present a summary of
97 the experimental results. In section 3, we present our theoretical framework: we describe the
98 specific properties of MgO in connection with first-principles density functional theory (DFT)
99 calculations [55, 56], and develop our "doorway model" for the last stage of the muon thermal-
100 ization and embedding in the crystal lattice. In section 4 we discuss the experimental findings
101 at the light of the doorway model and obtain the properties of the doorway state in MgO.
102 The main findings are summarized in section 5 and additional details of the experimental and
103 theoretical methods are presented in the appendix.

104 2 Experimental Results

105 MgO is an insulator with a bandgap of 7.8 eV [57], crystallizing in the face-centered cubic (fcc)
106 sodium chloride structure. Our sample was a commercial high-purity (> 99.99%) MgO single

107 crystal with dimensions $10 \times 10 \times 1 \text{ mm}^3$. The orientation of the sample was such that one of
 108 the axes pointed in the beam direction (flat side of the sample), and the other two axes were
 109 perpendicular to it in the horizontal and vertical direction. More details about the sample are
 110 given in section A.1 of the appendix.

111 The muon spin rotation (μ SR) experiment was performed at the Swiss Muon Source of the
 112 Paul Scherrer Institut in Switzerland [58] with the high-field spectrometer (HAL-9500) [59]
 113 in transverse geometry. A magnetic field $B = 1 \text{ T}$ was used. The magnetic field was applied
 114 parallel to the beam direction which means, considering the crystal orientation mentioned
 115 above, parallel to a cube axis of the fcc structure. The muon spin was rotated, before the im-
 116 plantation, from its original direction (antiparallel to the beam) towards the vertical direction
 117 to allow the transverse field measurement. Figure 1 shows the Fourier spectrum of μ SR data
 118 at $T = 6 \text{ K}$ and $B = 1 \text{ T}$.

119 The precession lines observed in the μ SR time spectra were analyzed with either a gaussian
 120 or a lorentzian relaxation function:

$$A(t) = A_0 \exp\left(-\frac{1}{2}\sigma^2 t^2\right) \cos(2\pi \nu t + \phi) \quad (1)$$

121 or

$$A(t) = A_0 \exp(-\lambda t) \cos(2\pi \nu t + \phi) \quad (2)$$

122 where A_0 , ν , ϕ , correspond to the amplitude, frequency and initial phase, and σ and λ to the
 123 relaxation rates, respectively. The fraction f of muons forming each configuration can be de-
 124 termined from comparison with the maximum instrumental asymmetry A_{max} determined from
 125 a silver calibration, as $f = A/A_{\text{max}}$. The experimental arrangement of the HAL-9500 spectrom-
 126 eter consisted of eight forward and eight backward detectors, arranged in rings around the
 127 muon beam. The detectors were combined to obtain a single parameter set (see section A.1
 128 of the appendix).

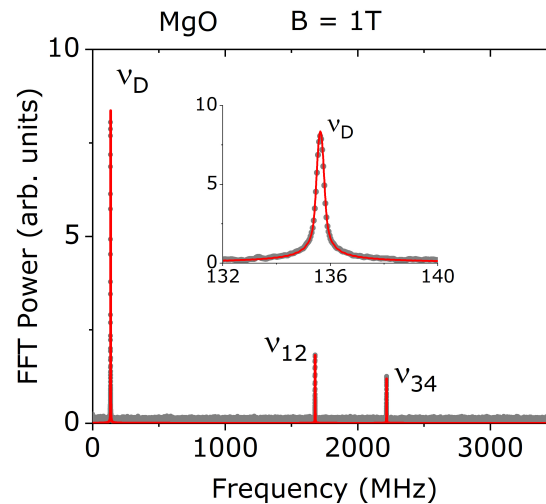


Figure 1: Fourier transform of the μ SR spectrum at temperature $T = 6 \text{ K}$ and a transverse magnetic field $B = 1 \text{ T}$. The diamagnetic-like component ν_D and the two components ν_{12} and ν_{34} of muonium are seen. The insert shows on an extended scale the broad diamagnetic-like line which is attributed to the doorway state (see text).

129 In μ SR experiments one can distinguish between two fundamentally different states, dia-
 130 magnetic or paramagnetic, by the different precession frequencies or relaxation of the muon
 131 spin polarization. Diamagnetic refers to the charged muonium state Mu^+ or Mu^- , where there
 132 is no interaction between the muon and an unpaired electron. When such an interaction is
 133 present, the configuration is called paramagnetic, designated as muonium (Mu^0) [17, 30]. If
 134 the hyperfine interaction of a paramagnetic state is very small, the apparent precession fre-
 135 quency is similar to that of the diamagnetic state and is therefore termed as "diamagnetic-like".

136 In Fig. 1, three lines, a diamagnetic-like line ν_D and the two paramagnetic components
 137 ν_{12} and ν_{34} of muonium are seen. The line at the muon Larmor frequency ν_D (shown on an
 138 extended scale in the insert) is broader than expected for a purely diamagnetic line, indicating
 139 that some paramagnetic interaction is present. We therefore call this line diamagnetic-like. It
 140 corresponds to the fast relaxing signal discussed in the literature [27, 31, 38]. A connection of
 141 these findings with the DFT calculations will be presented in section 3.

142 Figures 2, 3 and 4 summarize the experimental results. In Fig. 2 the results of the diamag-
 143 netic-like signal at $B = 1$ T are displayed as a function of temperature. The diamagnetic-like
 144 fraction (Fig. 2 a)), as calculated by comparing the asymmetry of the diamagnetic signal with
 145 the maximum instrumental asymmetry obtained from a Ag calibration sample, is approxi-
 146 mately constant (around 28%) up to about 100 K, then increases to about 42% at 300 K. The
 147 increase indicates a thermal activation of the formation of this state. The solid line is a fit as
 148 explained in section 4 (subsection 4.1).

149 The frequency of the diamagnetic-like signal (Fig. 2 b)) varies with temperature. The shift
 150 is very small, but significant. It is due to the paramagnetism of the electron which affects the

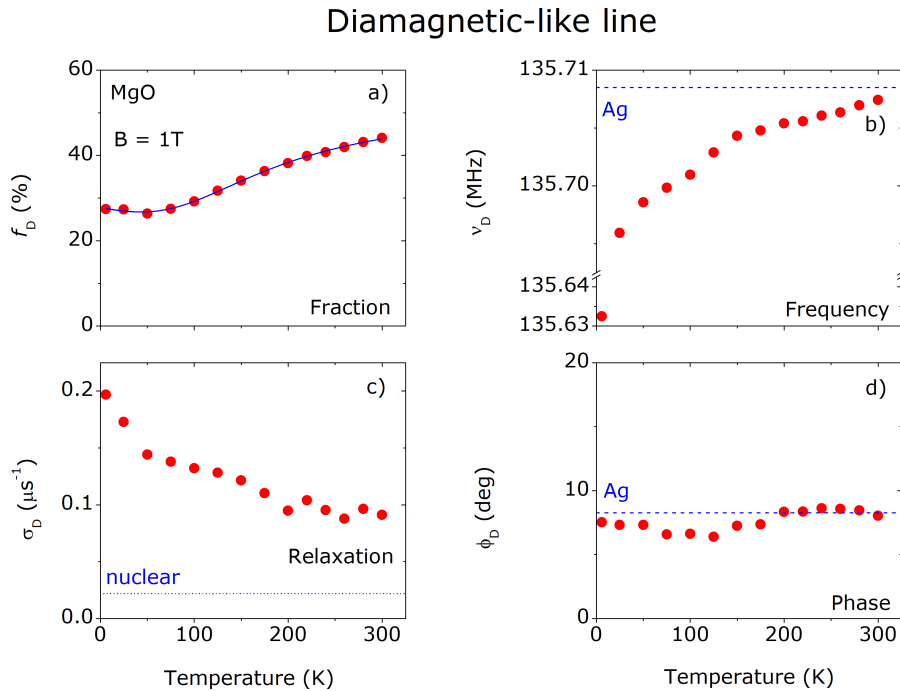


Figure 2: Temperature-dependence data (fraction f_D , relaxation σ_D , frequency ν_D and phase ϕ_D) of the diamagnetic-like signal in MgO at a nominal external applied magnetic field $B = 1$ T. Frequency and phase from a calibration with Ag are indicated as dashed blue lines in Fig. 2 b), and d). The dashed blue line in Fig. 2 c) corresponds to the calculated σ_D from nuclear magnetic moments. Note the interrupted vertical scale for the 6 K point in Fig. 2 b). The error bars are smaller than the size of the symbols.

151 muon spin via the hyperfine interaction.

152 The relaxation σ_D (Fig. 2 c)) is relatively small but clearly larger than the relaxation ex-
 153 pected from the interaction with nuclear spins only. The nuclear interaction (“nuclear” in the
 154 figure) was calculated [60,61] for the muon bound to an oxygen in the antibonding direction
 155 (see section 3 for details) and for the interaction of the muon spin with the nuclear moments
 156 of the spin-carrying isotopes of MgO. The increased relaxation indicates interaction with an
 157 electron.

158 The phase (Fig. 2 d)) corresponds approximately to that of the Ag calibration. No signifi-
 159 cance is attributed to the small variation with temperature.

160 Figure 3 shows the data for atom-like muonium in the high field ($B = 1$ T) experiment.
 161 Fig. 3 a) displays the amplitudes of the ν_{12} and ν_{34} signal. The difference of the amplitude
 162 values of the two lines is due to a frequency dependent time resolution factor which affects the
 163 amplitude of the higher frequency ν_{34} more than that of the lower frequency ν_{12} . The apparent
 164 peak in the amplitudes around $T = 100$ K will be discussed in connection with Fig. 4.

165 The hyperfine interaction A_{hf} (Fig. 3 b)) was obtained from the two frequencies via the
 166 diagonalization of the corresponding Hamiltonian [30]. The red solid line is a fit with an Ein-
 167 stein model with a single vibrational energy $h\nu$. In this model it is assumed that the change of
 168 A_{hf} is proportional to the mean square displacement $\langle u^2 \rangle$ of the atoms from the muon [63].
 169 For isotropic harmonic oscillator and Bose-Einstein statistics, the corresponding formula is:

$$A_{\text{hf}} = A_0 + \frac{C}{\exp\left(\frac{h\nu}{k_B T}\right) - 1} \quad (3)$$

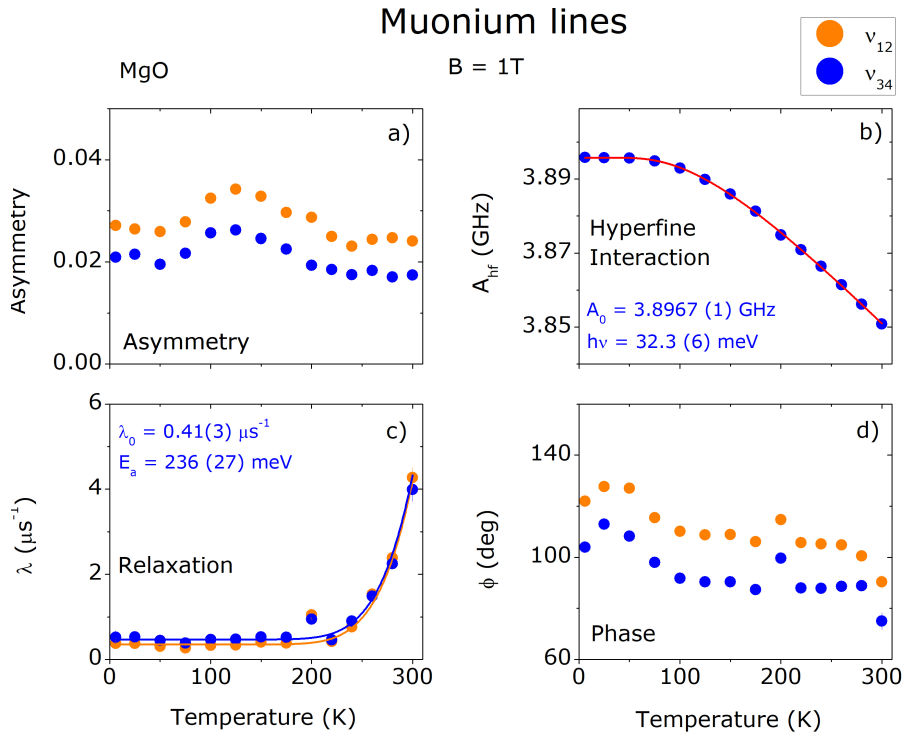


Figure 3: Temperature dependence of the two muonium lines ν_{12} and ν_{34} in MgO at $B = 1$ T. (a) Asymmetry of the two lines. (b) Hyperfine interaction A_{hf} deduced from the two frequencies. (c) Relaxation rates λ . (d) Initial precession phases ϕ for each line. The solid lines in (b) and (c) are fits as explained in the text. The obtained parameters are quoted in the figure. Most error bars are smaller than the size of the symbols.

170 The fit yields: $A_{\text{hf}}(T = 0 \text{ K}) = 3896.7(1) \text{ MHz}$ (corresponding to approximately 87% of
 171 the vacuum value) and $h\nu = 32.3(6) \text{ meV}$. The value of the vibrational energy is similar to that
 172 of an optical phonon in which atoms of the two sublattices vibrate against each other [64].

173 The relaxation rate λ (Fig. 3 c)) is approximately the same for both frequencies and con-
 174 stant at low temperatures. Above about 250 K, the relaxation increases. We performed a fit
 175 to both relaxations with common parameters with $\lambda = \lambda_0 + \lambda_1 \exp(-E_a/k_B T)$ and obtained
 176 $\lambda_0 = 0.38(3) \mu\text{s}^{-1}$ and $E_a = 236(27) \text{ meV}$. In the final fit, λ_1 was fixed to $3 \times 10^4 \mu\text{s}^{-1}$. It
 177 is unlikely that the increase of the relaxation with temperature is due to direct ionization of
 178 muonium, since the DFT calculations (see section 3, subsection 3.2) predict the $\text{Mu}^0 (+/0)$
 179 conversion level at 1.84 eV below the conduction band. The very fast increase of the relax-
 180 ation above 200 K is very untypical for trapping. Such a fast increase has been seen in many
 181 other systems in μSR and is indicative of a conversion of one state to another with very differ-
 182 ent hyperfine interactions [30,32]. We therefore suggest that the 236 meV activation energy is
 183 associated with the conversion of the interstitial muonium into a metastable bound configura-
 184 tion (doorway state, see section 3, subsection 3.4). The activation for this conversion requires
 185 less energy than the ionization of muonium without a configuration change.

186 Figure 3 d) shows the phase of the two frequencies at the instant $t = 0$. The time zero
 187 as defined by the spectrometer electronics does not necessarily coincide with the beginning
 188 of the muon spin rotation in the sample. This circumstance complicates the evaluation of the
 189 phase shift for high frequency lines. Because of the large uncertainties we have not further
 190 analysed the phases.

191 Figure 4 gathers the temperature dependence of the fraction of muons forming the diamag-
 192 netic-like signal (f_D , from Fig. 2 a)) and of the fraction of muons f_{Mu} forming the muonium
 193 state (from Fig. 3 a)), after correcting for the time-resolution effect, as explained in subsec-
 194 tion A.1 of the appendix. The muonium fraction f_{Mu} in Fig. 4 is obtained by summing the
 195 time-resolution corrected f_{12} and f_{34} Mu fractions obtained from Fig. 3 a). The intensity in
 196 the remaining two components ν_{23} and ν_{14} is negligible at this high field ($B = 1 \text{ T}$). The total
 197 fraction f_{tot} , the sum of f_D and f_{Mu} , is also shown in Fig. 4, as well as an extrapolation of the
 198 total fraction (corresponding to a fraction of 78%) obtained in a low-field experiment [62],

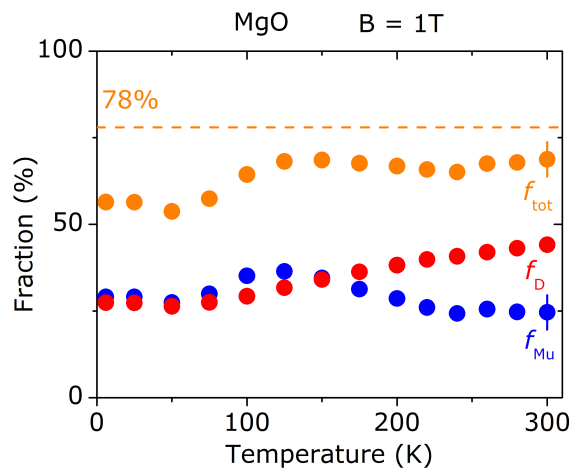


Figure 4: Temperature dependence of the fractions of muons forming the diamagnetic-like component f_D , the muonium component f_{Mu} , and the sum of the two f_{tot} . Also shown, as a dashed line, is the total fraction of 78%, obtained in a low field experiment ($B = 1.5 \text{ mT}$) at $T = 300 \text{ K}$, where no dephasing is observed [62]. The error bars at the last points of f_D and f_{tot} represent the uncertainty due to the time-resolution correction. Statistical errors are smaller than the size of the symbols.

199 where no dephasing was observed.

200 Broadened diamagnetic lines have been observed in the past in other systems and inter-
201 preted as shallow donor muonium states (see e.g. Ref. 65). The case in MgO is not different
202 from these previous cases and the properties of these states are similar to those observed in the
203 present MgO case. However, in the past works, no detailed information is given on the forma-
204 tion process and the geometrical structure of these states. In the present case we describe the
205 full history of this state from its formation to its decay and give the geometrical configuration
206 adopted at the different steps along this process.

207 3 Theory

208 3.1 Ab-initio (DFT) calculations

209 Muonium in MgO was investigated using density functional theory (DFT) calculations with
210 ab-initio pseudopotentials [66–68]. Exchange and correlation effects between the electrons
211 were described by the semilocal PBE functional [69] and the screened-exchange HSE06 hybrid-
212 functional approach [70, 71]. In these calculations, the muon particle is represented by a pro-
213 ton, an approximation that considers muonium to be the lighter pseudo-isotope of monatomic
214 hydrogen. This approximation is expected to yield nearly identical ground-state properties
215 for these species [20, 30]. Zero-point energies were explicitly treated in total energy barrier
216 calculations to account for the different isotopic masses. A more detailed description of the
217 DFT method can be found in subsection A.2 of the appendix.

218 Not only ground state but also metastable excited states were considered. They play a role
219 as intermediate configurations in implantation and doping processes. Electron configurations
220 are shown to demonstrate the interaction of hydrogen with the surrounding atoms. Energy
221 profiles along the diffusion path were calculated, both for frozen lattice and also accounting for
222 structural relaxation (relaxed lattice). The frozen lattice configuration is relevant for the fast-
223 diffusing particle, whereas the relaxed configuration represents the situation after stopping.

224 3.2 Muonium configurations in MgO

225 MgO crystallizes in the face centered cubic (fcc) sodium chloride structure (Fig. 5 a)). The
226 unit cell consists of cubes, each containing four Mg and four O atoms in the corners. Muons
227 with a kinetic energy of 4 MeV are implanted into this structure. In the end phase of the ther-
228 malization process, the resulting neutral muonium atom (Mu^0) (the muon has picked up an
229 electron during the slowing down process) diffuses through the lattice by hopping between
230 interstitial sites. The diffusion path is indicated by the arrow in Fig. 5 a). The final stable
231 configurations are: i) neutral muonium in the center of a cube (Fig. 5 b)) with the electron
232 density (in yellow) concentrated on the muon, and ii) ionized muonium Mu^+ bonded to an
233 oxygen atom (Fig. 5 c)). As mentioned in section 2, we assign the experimentally observed
234 muonium lines to the calculated neutral muonium state shown in Fig. 5 b). The purely ion-
235 ized muonium Mu^+ bonded to an oxygen atom (Fig. 5 c), is contained within the observed
236 diamagnetic-like line discussed in section 2.

237 The lowest-energy (ground state) site for neutral interstitial muonium is in the center of a
238 cube. Examination of the ground-state charge density for this defect shows that the muonium
239 electron has a strong 1s-type spherically symmetric character and it is centered at the muon
240 site (see Fig. 5 b)). Some residual finite spin density exists also at the four neighboring oxy-
241 gen atoms of the cube. This suggests that muonium polarizes to some degree its immediate
242 environment. The calculated hyperfine interaction is dominated by an isotropic term, A_{iso} .
243 The magnitude of A_{iso} obtained by the hybrid HSE06 functional is approximately 91% of the

244 vacuum value, in reasonable agreement with the experimental value for muonium (87%) (see
 245 section 2). In addition to this state, muonium forms a bound configuration where the muon
 246 is displaced from the cube center and forms a O–Mu bond in analogy to the hydroxyl O–H
 247 type bond (Fig. 5 c). This O–Mu bound configuration was found by the DFT calculations to
 248 be thermodynamically stable solely in its positively-charged state. The (+/0) conversion level
 249 was found to lie deep in the gap, at 1.84 eV below the conduction-band edge.

250 3.3 Diffusion barrier for muonium migration

251 Towards the end of the thermalization process, muonium diffuses with the remaining kinetic
 252 energy from one interstitial site to the next through the square plane between the two sites
 253 (Fig. 5 a). On symmetry grounds, the lowest energy path is through the center of this plane,
 254 which corresponds to the highest point of the energy barrier between the stable positions at
 255 the center of the cubes. The calculated energy profile and corresponding electron-densities
 256 are displayed in Fig. 6. It can be seen that muonium retains its strong atomic character for
 257 large portions along the path. The energy maximum occurs at the midpoint of the path when
 258 the nucleus occupies the face center position, which is the saddle point of the diffusion path.
 259 The energy barrier for such a path was obtained under two different assumptions. First, by
 260 taking a frozen-lattice approximation using the HSE06 lattice parameter (equal to 4.14 Å)
 261 for the bulk-crystalline $2 \times 2 \times 2$ MgO supercell. The underlying assumption here is that the
 262 ions of the host remain fixed at their equilibrium lattice sites of the unperturbed pristine MgO
 263 crystal during the hydrogen/muonium migration. This approximation does not, therefore,
 264 consider structural relaxation effects. Alternatively, under the relaxed-lattice approximation
 265 these effects are explicitly treated by allowing the nearest neighbors of the diffusing species
 266 to displace and adjust their position during the migration process. Additional calculations
 267 by allowing all atoms to relax led to very small modifications of the migration barrier (\approx

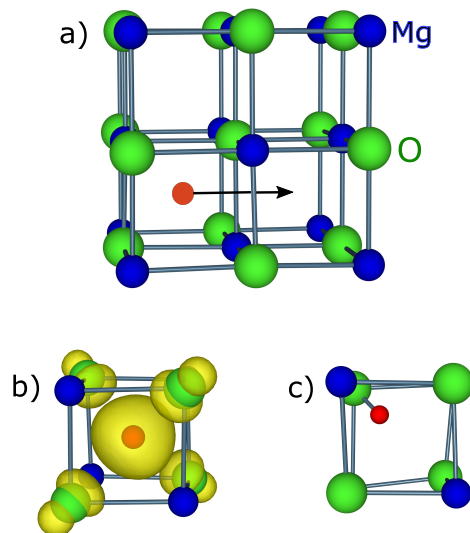


Figure 5: a) Sodium chloride structure of MgO. Also indicated is the position of the muonium (red sphere) in the center of the cube and the expected diffusion path from one cube to the next (arrow). b) Calculated (DFT) position of neutral muonium in the center of the cube (red dot) and the electron-spin distribution around the muon (yellow cloud). c) Calculated (DFT) position of the positive muonium (Mu^+) bound to an oxygen atom.

268 0.02 eV), suggesting that the barrier magnitude is mainly controlled by the nearest-neighbor
 269 interactions.

270 The results show a strong effect of structural relaxation on the barrier height (see Fig. 6).
 271 A rather high barrier of 1.83 eV is observed in the frozen-lattice approximation. This is due to
 272 strong overlap interactions between the diffusing hydrogen/muonium and its neighbors; at the
 273 saddle point (the top of the barrier), the two nearest Mg and O neighbors are 1.46 Å apart from
 274 the muon. Taking relaxation effects into account, the migration barrier drops significantly to
 275 0.64 eV, with the four nearest neighbors moving away from the muon and eventually reaching
 276 a distance of 1.63 Å.

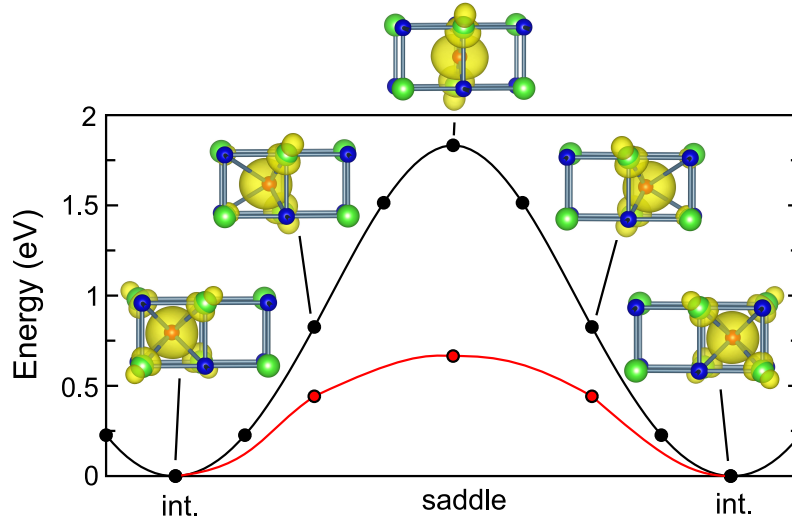


Figure 6: DFT energy profile and electron densities for intermediate muonium positions along the diffusion path of muonium from one cube center to the next through the common cube face: black line for the non-relaxed frozen lattice; red line for the relaxed lattice. The path of the muon is indicated. The points were calculated with the HSE06 functional, the lines are guides to the eye.

277 The barrier profiles shown in Fig. 6 are without consideration of the zero-point energy
 278 of the particle. A change in barrier height can occur if the zero-point energy is different in
 279 the ground state and in the saddle-point configuration. This can have an appreciable effect
 280 for the relatively light muonium particle. The zero-point energy correction to the migration
 281 barriers was determined here by calculating the local vibrational contributions of the muon
 282 particle [72]. These calculations were performed within a harmonic approximation for the
 283 muon motion which should be sufficient for obtaining the migration barriers at the low tem-
 284 peratures (< 300 K) examined in the present study. Our calculations show that zero-point
 285 effects are negligible in the frozen-lattice results because the respective sums of the vibra-
 286 tional frequencies in the two sites cancel. However, for the relaxed geometry, a softening of
 287 the vibration frequencies by about 35% at the saddle point leads to a considerable reduction
 288 of the migration barrier of muonium by 190 meV, lowering the final barrier to 0.45 eV. Over-
 289 all, the final theoretical barrier is in acceptable agreement with the experimentally extracted
 290 activation energy of site conversion (236 meV) (see section 2).

291 3.4 The doorway model

292 We develop here a model for the last stage of the thermalization of the implanted muon into the
 293 lattice. Since the whole process begins with a specific reaction through which the final embed-
 294 ding process proceeds, we call it doorway model. The "doorway state" concept has been used

295 extensively in nuclear physics to describe intermediate structures in nuclear reactions [73].
 296 The model has also been applied in other connections, e.g. in fullerene research, where the
 297 excitation of vibrational modes occurs via the primary excitation of a particular oscillation [74].

298 The muon leaves the charge exchange regime as neutral muonium Mu^0 or as positive
 299 charged Mu^+ [26]. The formation of Mu^- is very unlikely at this stage. The kinetic energy
 300 of the muon after the charge exchange regime is in the order of 1 to several eV, related to
 301 the band gap of the host material [25, 26]. The present experimental observations of a large
 302 relaxation and frequency-shift of the diamagnetic-like signal in Fig. 2 reveal the paramagnetic
 303 character of the state. This clearly indicates that, at the end of the charge-exchange process,
 304 the energetic neutral muonium Mu^0 configuration is present in this case. We will therefore
 305 now discuss the reaction of the neutral muonium fraction with the lattice.

306 After the charge exchange stage, the neutral muonium moves with the remaining kinetic
 307 energy from interstitial site to interstitial site across a potential barrier. Initially, the site
 308 changes are so fast that the lattice atoms cannot react and the muonium diffuses in the pristine
 309 (non-relaxed) lattice. The muonium loses kinetic energy through elastic scattering at the host
 310 atoms until the energy becomes so low that the muonium barely reaches the barrier height. In
 311 this case, the residence time at the top of the barrier is long enough to allow a strong inelastic
 312 reaction with the host atoms. More details will be discussed below. The proposed mechanism
 313 for the muon reaction with the host lattice is sketched in Fig. 7.

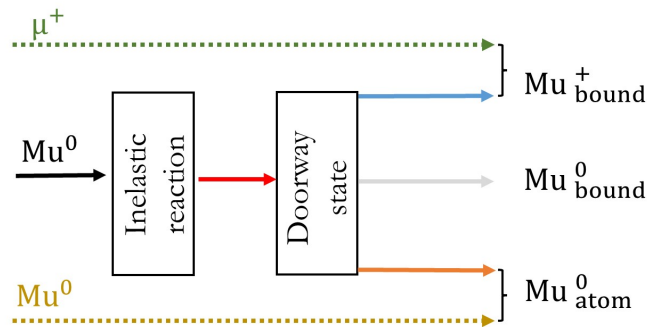


Figure 7: Flow diagram of the reaction of the muon with the host lattice at the final stage of thermalization. The middle part of the figure (solid lines) sketches the doorway reaction mechanism: incoming neutral muonium is stopped by the excitation of a local vibration of the surrounding atoms (inelastic reaction). The resulting composite configuration, the doorway state, lasts for some time (ns to μs) before decaying into either atom-like neutral muonium ($\text{Mu}_{\text{atom}}^0$) or a positively charged bound state ($\text{Mu}_{\text{bound}}^+$). In general, a neutral bound configuration ($\text{Mu}_{\text{bound}}^0$) can also be formed, but this is not the case here. There are two side reactions (indicated by dotted lines): μ^+ at the end of the charge-exchange regime may react directly with the host atoms forming $\text{Mu}_{\text{bound}}^+$. Or neutral muonium can be stopped by elastic scattering only, without the strong inelastic process, forming directly $\text{Mu}_{\text{atom}}^0$.

314 The middle part of Fig. 7 shows the doorway mechanism with the inelastic reaction and
 315 the formation and decay of the doorway state. This part will be discussed in detail below.
 316 But we would like to mention before that two other embedding reactions are possible. It
 317 is possible that at the end of the charge-exchange regime, μ^+ is integrated directly into the
 318 lattice (top dashed line in Fig. 7). Another possible reaction could be that the neutral energetic
 319 muonium at the end of the charge-exchange regime is stopped by elastic scattering only and
 320 passes directly to the atomic ground state (bottom dashed line in Fig. 7). In the present case of

321 MgO, these competing reactions seem to be of minor importance, but in other semiconductors
322 and insulators they may be significant.

323 *Inelastic reaction.* The inelastic reaction is caused by the force exerted by the squeezed
324 muonium on the surrounding atoms. A rough estimate that the reaction can take place is that
325 the residence time τ of the muonium at the top of the barrier is of the order of the inverse
326 phonon frequency ν : $\tau \approx 1/\nu$. If a frequency at the upper end of the phonon spectrum [64] is
327 assumed for this local vibration ($\nu \approx 10^{13} \text{ s}^{-1}$), this results in a value in the order of 10^{-13} s for
328 the dwell time of the muonium at the top of the barrier. This condition is fulfilled if the muo-
329 nium has no more than a few meV kinetic energy over a length of about the Bohr radius of the
330 muonium (0.054 nm). Of course, these classical considerations give only order of magnitude
331 values.

332 *The doorway state.* Immediately after the inelastic process, the muon is still at the position
333 it was before the reaction, i.e. in the center of the cube surface (Fig. 6), but the neighboring
334 lattice atoms are now vibrating. We call this strongly excited phase, which lasts only nanosec-
335 onds or less, the "thermal spike" regime. Due to the coupling of the initial excitation to other
336 phonon modes, the spike energy diffuses rapidly into the lattice and a relaxed configuration is
337 formed [33]. This situation lasts up to hundreds of nanoseconds long and is thus observable
338 on the timescale of μSR . The muonium state in the hot phase ("thermal spike" regime) and
339 the subsequent relaxed configuration constitute what we call the "doorway state". We there-
340 fore define the doorway state as comprising the two phases, the short-lived hot phase and the
341 longer-lived relaxed phase. This latter state is accessible to muon spectroscopy.

342 4 Discussion

343 4.1 Formation and decay of the doorway state

344 *Formation of the doorway state.* Immediately after the inelastic reaction, the muonium is in a
345 agitated environment. In this early phase, reactions to the final states can already take place,
346 and only a part remains in the doorway configuration, now with relaxed surroundings. We
347 use the term "long-lived doorway state" for this longer-lived part, bearing in mind that there is
348 a short-lived precursor hot stage in which reactions to the final states can already take place.

349 The doorway state lasts for hundreds of nanoseconds and is thus accessible for μSR spec-
350 troscopy. The lifetime of the long-lived state can not be determined precisely here because
351 we can not separate exactly the slightly paramagnetic doorway state from the fully diamag-
352 netic state which is the final state arising from the conversion. The fact that the paramagnetic
353 interaction is seen in μSR indicates that the doorway state exists at least some time during
354 the lifetime of the muon ($2.2 \mu\text{s}$). A similar case is the fast relaxing signal in Al_2O_3 [38, 75].
355 There, lifetimes (inverse conversion rates) of about $1 \mu\text{s}$ were observed at low temperatures.
356 The lifetime decreases rapidly above about 40 K and reaches a value of about 5 ns at about
357 room temperature. A similar behaviour is expected here, but the actual values depend on the
358 material.

359 We identify the long-lived doorway state with the fast-relaxing part of the diamagnetic-like
360 signal in the experiment (shown in Fig. 2 and repeated in Fig. 8 a)). As mentioned before,
361 the diamagnetic-like signal contains also a contribution from the purely diamagnetic Mu^+
362 configuration which cannot be separated in the present experiment. This has to be kept in
363 mind when discussing the final results. The diamagnetic-like fraction will now be analyzed in
364 detail.

365 The increase in the diamagnetic-like fraction in Fig. 8 a) above 100 K indicates that the
366 formation of this configuration needs thermal activation. The fact that the fraction does not

367 decrease further below 100 K is attributed to the thermal spike, which has a similar effect as
 368 an increased temperature. For the thermal spike temperature, T_{spike} , we assume an inverse
 369 S–shape temperature dependence with parameters T_0 , $T_{1/2}$ and k [33]:

$$T_{\text{spike}} = \frac{T_0}{1 + \exp[k(T - T_{1/2})]} \quad (4)$$

370 We then define an effective temperature $T_{\text{eff}} = T_{\text{spike}} + T$ and describe the diamagnetic-like
 371 fraction f_D by:

$$f_D = f_0 \frac{N \exp\left(-\frac{E_a}{k_B T_{\text{eff}}}\right)}{1 + N \exp\left(-\frac{E_a}{k_B T_{\text{eff}}}\right)} \quad (5)$$

372 where E_a is the activation energy, N the statistical weight factor and f_0 the total fraction. The
 373 fit result is shown in Fig. 8 a) as a solid line. The effective temperature T_{eff} is represented
 374 in Fig. 8 b), together with T_{spike} and T . The few experimental points in the low temperature
 375 range do not allow a clear separation between the thermal spike and the lattice temperature
 376 contribution. Since the experimental diamagnetic fraction is approximately constant below
 377 about 100 K, we have adjusted the spike temperature parameters to obtain an approximately
 378 constant effective temperature below 100 K. The fit was then performed with fixed parameters
 379 for T_{spike} : $T_0 = 120$ K, $T_{1/2} = 47$ K and $k = 0.038$ K⁻¹. The parameters of the thermal spike
 380 are effective values simulating the muonium reaction in the hot phase. T_0 is approximately
 381 the effective temperature at the muon site at $T = 0$ K. The $T_{1/2}$ value of 47 K indicates that
 382 the thermal spike effect gradually disappears around this temperature; k describes the slope
 383 of the decrease with temperature.

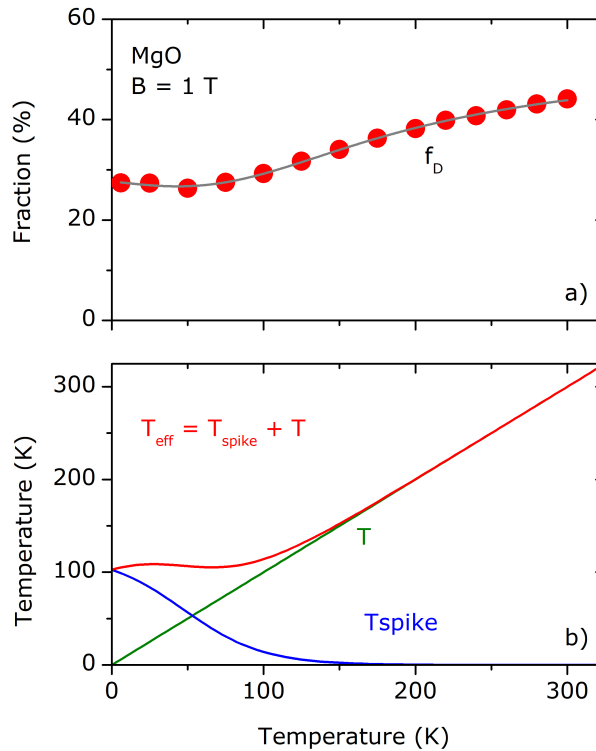


Figure 8: a) Diamagnetic-like fraction (points) and fit with Eq. 4 (solid line). b) Effective temperature T_{eff} composed of the thermal spike temperature T_{spike} and lattice temperature T .

384 In the final fit, f_0 was fixed to 78%, the value obtained in the low field experiment at higher
 385 temperatures [62]. The results yield $E_a = 12(1)$ meV and $N = 2.0(1)$. Thus there is a small
 386 barrier for the formation of the diamagnetic-like configuration but the higher statistical weight
 387 ($N \approx 2$) causes that diamagnetic-like fraction to increase with increasing temperature.

388 *Decay of the long-lived doorway state.*

389 The decay of the long-lived doorway state is schematically sketched in Fig. 9. It decays
 390 either to atom-like interstitial muonium Mu^0 or to a bound configuration where, in the present
 391 case, the muon is bound to an oxygen atom in a diamagnetic Mu^+ configuration and the
 392 electron is in the conduction band. The sketch at the top of Fig. 9 indicates the site change
 393 of the muon from the middle of the square plane to either the center of the cube or to a
 394 bound configuration with an oxygen atom. The bottom pictures in Fig. 9 display the finally
 395 formed configurations: atom-like muonium Mu^0 with the electron distribution around it and
 396 the diamagnetic Mu^+ bound to an oxygen atom.

397 The long-lived doorway state decays mainly by the loss of the electron. In the present case,
 398 the electron distribution appears to spread out more and more with increasing temperature,
 399 reducing the hyperfine interaction until the interaction disappears completely and a purely
 400 diamagnetic state is formed.

401 In principle, the long-lived doorway state could also decay to atomic muonium (see Fig. 9).
 402 However, the observed muonium lines cannot stem from this decay since dephasing due to

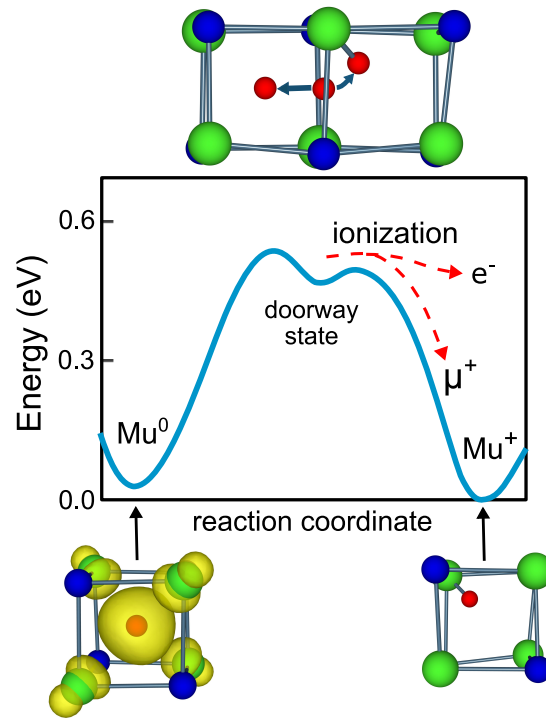


Figure 9: Schematic potential profile for muonium in the long-lived doorway state, in MgO. The decay of the long-lived doorway state occurs either to interstitial muonium, Mu^0 , or to a bound configuration in which the muon is bound to an oxygen atom in the diamagnetic Mu^+ configuration and the electron e^- is in the conduction band (CB). The left side of the potential curve and the energy scale are taken from the potential obtained for muonium diffusion in the relaxed lattice (red curve in Fig. 6), the right side is only schematic. The symbols indicate: green O, blue Mg, red μ^+ and yellow the electron cloud.

403 the transition from the diamagnetic-like frequency to the muonium frequencies and the long
 404 conversion time (hundreds of nanoseconds) would destroy the phase coherence completely.
 405 But some muonium fraction from this decay may be contained in the missing fraction (see
 406 Fig. 4). The main part of the observed muonium is most likely formed in the short-lived
 407 (nanoseconds or less) thermal spike phase.

408 The missing fraction has two contributions: one refers to the polarization loss in the hot
 409 phase directly after the stopping of the muon. It accounts for the fraction loss from 100%
 410 to 78% fraction which is seen in the low field experiment where no phase shift is observed.
 411 The second part is attributed to dephasing in the transition of the intermediate state to the
 412 interstitial atomic configuration. It accounts for the fraction loss between 78% and the total
 413 fraction.

414 4.2 Properties of the long-lived doorway state

415 Paramagnetic interaction I: Hyperfine interaction derived from the line width

416 The measured relaxation rate (linewidth in frequency space) is larger than expected if only
 417 nuclear moments were causing the line broadening. To obtain the electronic contribution
 418 alone (Fig. 10), the nuclear contribution was subtracted via $\sigma_{el} = \sqrt{\sigma_D^2 - \sigma_{nuc}^2}$. Here σ_D is
 419 the measured diamagnetic-like relaxation and σ_{nuc} the nuclear contribution which was cal-
 420 culated [60, 61] for the muon configuration shown in Fig. 5 c). The calculated value of the
 421 nuclear interaction is $\sigma_{nuc} = 0.02 \mu s^{-1}$.

422 The hyperfine interaction obtained in this way has values on the order of a few 100 kHz
 423 (right scale in Fig. 10). These very small values (about five orders of magnitude smaller than
 424 those of the interstitial muonium) indicate that the electron is widely distributed and has very
 425 little overlap with the muon.

426 The hyperfine interaction (right scale in Fig. 10) decreases continuously with increasing
 427 temperature from about 450 kHz to about 120 kHz. One reason for this is electron spin fluc-
 428 tuation, which changes the sign of the interaction leading to a narrowing of the line. Another

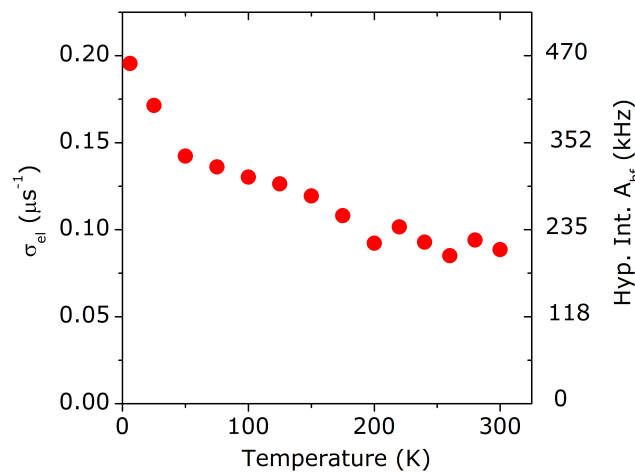


Figure 10: Electronic part of the relaxation σ_{el} of the diamagnetic-like component, obtained by subtracting the nuclear contribution. The right scale shows the hyperfine interaction derived from the linewidth via $A_{hf} \approx FWHM \approx 2.35 \sigma_{el}$. We attribute the electronic part of the relaxation rate to the presence of an unresolved hyperfine interaction A_{hf} .

429 possibility is that the electron moves further outward with increasing temperature, reducing
 430 the residence time at the muon site. Eventually, the electron may be lost completely, leaving
 431 Mu^+ behind. In the present case of MgO, it is not possible experimentally to separate the
 432 slightly paramagnetic and the purely diamagnetic state.

433 Paramagnetic interaction II: Frequency shift at high field ($B = 1$ T)

434 The frequency shift at high fields (Fig. 2 b)) is caused by the polarization of the electron spin
 435 and is large only at high fields and low temperatures. For unresolved hyperfine lines, we
 436 can assume that the frequency shift $\Delta\nu$ is given by the average frequency of the two lines
 437 weighted by their intensities. The line intensities are given by the polarization of the electron
 438 spin $P_e(B, T)$, which depends on the field B and the temperature T . Assuming thermodynamic
 439 equilibrium for the electron spin, one obtains

$$\Delta\nu = \frac{A_{\text{hf}}}{2} P_e(B, T) = \frac{A_{\text{hf}}}{2} \tanh\left(\frac{\mu_B B}{k_B T}\right) \quad (6)$$

440 Here A_{hf} is the hyperfine interaction, μ_B the Bohr magneton and k_B the Boltzmann con-
 441 stant. With the approximation $\tanh x \approx x$ for small x , one obtains:

$$\begin{aligned} \frac{\Delta\nu}{\nu} &= \frac{\gamma_e}{\gamma_\mu} \frac{hA_{\text{hf}}}{4k_B T} = (248.6 \times 10^{-11} \text{ K.s}) \frac{A_{\text{hf}}(\text{s}^{-1})}{T(\text{K})} \\ A_{\text{hf}}(\text{s}^{-1}) &= 0.4 \times 10^9 \frac{\Delta\nu}{\nu} T(\text{K}) \end{aligned} \quad (7)$$

442 Fig. 11 shows the relative frequency shift $\Delta\nu/\nu$, normalized to the Ag calibration, on the
 443 left scale, and $\Delta\nu'/\nu$ normalized to the asymptotic behaviour at high temperatures, at the
 444 right scale (see the following discussion). Since the shifts are very small (in the ppm range),

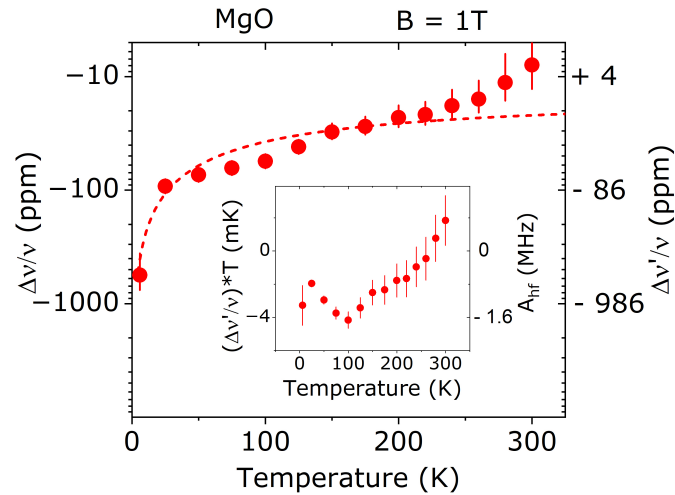


Figure 11: Relative frequency shift at $B = 1$ T as a function of temperature: the left scale shows $\Delta\nu/\nu$ normalized to the Ag calibration, the right scale shows $\Delta\nu'/\nu$ normalized to the asymptotic behavior, assuming that the shift is zero at high temperatures. The dashed line is a fit with a $1/T$ dependence (Eq. 7). The insert shows $(\Delta\nu'/\nu) \times T$ on the left and the corresponding hyperfine interaction A_{hf} on the right.

445 a close look at the errors is appropriate: the statistical error of the frequency measurement is
446 about 1 – 2 ppm. The temperature dependence measurements between 25 K and 300 K were
447 made in a single run without changing the field. The stability of the magnet is in the ppm
448 range, so the magnet instability does not contribute to the error. The 6 K point was measured
449 in a different run. Since the reproducibility of the field setting may have a large error, we did
450 not include this point in the fitting procedure, but included the point in the final plot.

451 We first fitted the data normalized to the Ag calibration (left scale in Fig. 11) with a $1/T$
452 dependence (Eq. 7), but allowed a constant offset. The result yielded an offset of -14(5) ppm.
453 On the right scale of Fig. 11 we represent the relative shift $\Delta\nu'/\nu$, corrected for this fitted
454 offset. This corresponds to a normalization of the frequency shift to the asymptotic behavior
455 at high temperatures where no shift is expected. For the data between 25 K and 300 K, we
456 assumed an error of 5 ppm (corresponding to the uncertainty in the offset), whereas for the
457 6 K point an estimated error of 200 ppm was adopted.

458 As can be seen in Fig. 11, the frequency shift is negative. Since the electron polarization
459 is positive, the hyperfine interaction must be negative. Negative hyperfine interactions are
460 not uncommon for bonded muonium configurations, as observed, for example, for the contact
461 term of bond-centered muonium in group IV elements [30].

462 The hyperfine interaction derived from the corrected $\Delta\nu'/\nu$ frequency shift is of the order
463 of 1 – 2 MHz in the low-temperature range (see insert of Fig. 11). At higher temperatures, the
464 errors are very large and no reliable values of hyperfine interaction can be extracted. The value
465 obtained at low temperatures is much larger than the hyperfine interaction obtained from the
466 linewidth (Fig. 10), where values of the order of a few 100 kHz were measured. This apparent
467 discrepancy can be explained as follows: i) the linewidth measures the *average* value of the
468 hyperfine splitting. Electron spin fluctuations narrow the splitting. ii) On the other hand, the
469 frequency shift measures the *position* of the average value, which depends on the intensity of
470 the two hyperfine lines. The fluctuations keep (or even establish if not already present) the
471 thermodynamical equilibrium occupation of the hyperfine lines.

472 Thus, the measured frequency shift gives the *actual* hyperfine splitting, while the linewidth
473 yields the *average* value for the fluctuating electron spin. The hyperfine interaction displayed
474 in the inset to Fig. 11 shows some variation with temperature. These could be real effects, but
475 the errors are large, so we do not discuss this further. We note that the fit in Fig. 11 clearly
476 only describes the gross variation of the relative frequency shift and that other minor effects
477 may be playing a role. The present data do not allow however for a more detailed analysis.

478 5 Conclusions

479 In the present study, combining μ SR measurements and DFT calculations, detailed information
480 about the reaction of muonium with the host lattice in MgO is obtained. The experimental
481 data are well described by a model that we call "doorway model". The basic assumption of
482 this model is that neutral muonium is stopped at the end of the implantation path by a strong
483 inelastic process. The inelastic reaction occurs at the top of the diffusion barrier, where the
484 muonium is slow enough to excite a local vibration. This excitation is not caused by the impact
485 of the moving particle, but by the expansion force of the compressed muonium. After this
486 reaction, the muon is stopped, and a compound system is formed which decays independently
487 from its formation. First a short-lived hot phase and subsequently a longer-lived relaxed phase
488 are formed. This latter state ("long-lived doorway state") is accessible to muon spectroscopy.

489 The long-lived doorway state is characterized by a widespread electron distribution around
490 the oxygen-bound muon with an average hyperfine interaction in MgO on the order of a few
491 100 kHz. The momentary hyperfine interaction is in the order of 1 to 2 MHz but is reduced

492 to a smaller average value by electron spin fluctuation. The presence of the electron in the
493 diamagnetic-like long-lived doorway state is evidenced by the line broadening and by the
494 frequency shift of the diamagnetic-like line. The negative value of the paramagnetic shift
495 indicates that the sign of the hyperfine interaction is negative. The paramagnetic interaction
496 is observed up to temperatures above 300 K, suggesting that the electron remains bound to
497 the muon in MgO beyond 300 K.

498 MgO is a favorable case for these investigations due to its simple lattice structure and low
499 density of nuclear magnetic moments, allowing a clear observation of the electronic interac-
500 tion. We expect that the doorway model can be applied, at least in part, to μ SR studies of
501 other semiconductors and insulators.

502 Acknowledgements

503 Muon beam time allocation from the Laboratory for Muon-Spin Spectroscopy at the Paul Scher-
504 rer Institut and the support of the PSI muon team are gratefully acknowledged. Technical
505 assistance from Dr. Tatsuo Goko is particularly acknowledged. The authors also acknowledge
506 the use of the computing facilities of CFisUC and the Department of Physics of the University
507 of Coimbra. A. W. thanks Prof. Klaus Lips for support of this work.

508 **Funding information** This work was financed through national funds by FCT - Fundação
509 para a Ciência e Tecnologia, I.P. in the framework of the projects UIDB/04564/2020 and
510 UIDP/04564/2020, with DOI identifiers 10.54499/UIDB/04564/2020 and
511 10.54499/UIDP/04564/2020, respectively.

512 A Methods

513 A.1 Experimental details and methods

514 The sample was a commercial high-purity ($> 99.99\%$) MgO single crystalline substrate from
515 Alfa Aesar, with dimensions $10 \times 10 \times 1 \text{ mm}^3$. The crystallographic orientation of the sample
516 was such that one of the axes pointed in the beam direction, and the other two axes were per-
517 pendicular to it in the horizontal and vertical direction. This was checked by X-ray diffraction,
518 which also confirmed the high crystalline quality of the sample.

519 The μ SR experiment was performed at the Swiss Muon Source of the Paul Scherrer Institut
520 in Switzerland [58] with the high-field spectrometer (HAL-9500) [59] in transverse geometry.
521 A magnetic field $B = 1 \text{ T}$ was used. The magnetic field was applied parallel to the beam
522 direction which means, considering the crystal orientation mentioned above, parallel to a cube
523 axis of the fcc structure. The muon spin was rotated, before the implantation, from its original
524 direction (antiparallel to the beam) towards the vertical direction to allow the transverse field
525 measurement.

526 The muons are implanted into the sample with energy of about 4 MeV and stop well in-
527 side the sample (a few hundred μm below the surface). The muon spin rotation (μ SR) is
528 measured by detecting the anisotropic emission of positrons as a function of time [17, 18].
529 The experimental arrangement of the HAL-9500 spectrometer consisted of eight forward and
530 eight backward positron detectors, arranged in rings around the muon beam. Data analysis
531 was performed using the Musrfit [76] and WiMDA [77] software.

532 Figure 1 shows the Fourier spectrum of μ SR data at $T = 6 \text{ K}$ and $B = 1 \text{ T}$. Three lines, a
533 diamagnetic-like line and the two components ν_{12} and ν_{34} of muonium are seen. The data

534 were therefore analysed with three relaxing components, as follows

$$\begin{aligned}
 A(t) = & A_D \exp\left(-\frac{1}{2}\sigma_D^2 t^2\right) \cos(2\pi\nu_D t + \phi_D) + \\
 & + A_{12} \exp(-\lambda_{12} t) \cos(2\pi\nu_{12} t + \phi_{12}) + \\
 & + A_{34} \exp(-\lambda_{34} t) \cos(2\pi\nu_{34} t + \phi_{34})
 \end{aligned}
 \tag{A.1}$$

535 where A_i , ν_i , ϕ_i represent the corresponding amplitude of the oscillation, precession frequency
 536 and initial phase, respectively; the index $i = D, 12$ or 34 indicates the diamagnetic-like line,
 537 the muonium 12 line and the muonium 34 line, respectively; λ_i and σ_i represent the spin
 538 relaxation rates, which have been found in a preliminary analysis to be better described by
 539 a lorentzian shape for the muonium lines and by a gaussian shape for the diamagnetic line.
 540 A global fit was performed for all sixteen detectors of the HAL9500 instrument, where the
 541 number of positron counts in each detector was fitted to $N_i(t) = N_i^0 \exp(-t/\tau_\mu)[1 + A_i(t)]$,
 542 with $A_i(t)$ given by Eq. A.1, τ_μ the muon lifetime and N_i^0 the normalized number of counts
 543 for each detector. Thereby the frequency and relaxation rate were assumed to be the same
 544 for all detectors, but the phases were left free. The fractions of muons forming each state
 545 were obtained by comparing with the maximum instrumental asymmetry A_{\max} obtained from
 546 a calibration measurement with silver.

547 As mentioned above, the eight forward as well as the eight backward detectors were ar-
 548 ranged on a ring around the beam direction. The nominal rotation angle between two adjacent
 549 forward or backward detectors is thus approximately 45° . The fits with individual phases for
 550 each detector gave indeed a phase difference between two adjacent detectors of 45° within
 551 1° variation. We therefore performed also fits with fixed relative phases of 45° , and a phase
 552 difference between a reference forward detector and a reference backward detector. These fits
 553 gave the same chi-squares as the fits with free phases. Therefore, the final analysis was per-
 554 formed with fixed relative phases with respect to the phase of the reference detectors. By this
 555 procedure only a single effective phase is obtained for each frequency.

556 A.1.1 Correction for time resolution.

557 For high-frequency lines, the finite time resolution reduces the observed amplitude. A gaussian
 558 dependence on the frequency ν is assumed for the correction function $C(\nu)$:

$$C(\nu) = \exp\left[-(2\pi\nu\sigma)^2/2\right] \tag{A.2}$$

559 For the width σ , the value $\sigma = 86$ ps from Ref. 59 was adopted. All amplitudes, including
 560 those of the Ag calibration, were corrected for this effect. For the diamagnetic component f_D ,
 561 the correction due to the time resolution has no effect, but the muonium lines are strongly
 562 affected. The uncertainty due to the correction is shown as an error bar in Fig. 4.

563 A.2 DFT calculations: Setup and preliminaries

564 The DFT calculations were carried out by the *ab-initio* VASP code [66–68]. The corresponding
 565 implementation is based on the projector augmented-wave method [78, 79] and the use of
 566 pseudopotentials to represent the core-valence interactions. Accordingly, the valence-electron
 567 wavefunctions were expanded by taking a plane-wave basis limited by a cutoff of 440 eV.
 568 Exchange and correlation effects between the electrons were described by the semilocal PBE
 569 functional [69] as well as by the HSE06 hybrid-functional approach which includes a fraction
 570 of 35% of exact non-local exchange [70, 71]. The hyperfine constants for the neutral hydrogen
 571 (muonium) states were determined by adopting the approach in Ref. [80].

572 Whereas the PBE functional gives a very low energy band gap (equal to 4.98 eV), the
573 latter approach instead yields a gap equal to 7.92 eV in excellent agreement with the reported
574 experimental gap, 7.8 eV, of MgO [57].

575 For the defect calculations the hydrogen/muon particle was treated as an impurity and was
576 embedded inside $2 \times 2 \times 2$ (64-atom) bulk-crystalline MgO supercells. Minimization of the total
577 zero-temperature internal energies led to the formation energies and charge-transition levels
578 for all possible hydrogen/muonium configurations [81]. This treatment should be sufficiently
579 accurate for low temperatures (less than 300 K) where the present μ SR measurements were
580 performed with anharmonic effects expected to be negligible [82]. The final results of these
581 quantities reported in the present study were obtained by means of the HSE06 functional.

582 Migration-energy profiles were determined by means of a constrained-path approach [83].
583 The energy barriers were obtained both for the frozen lattice and also accounting for structural
584 relaxation along the diffusion paths (relaxed lattice).

585 References

- 586 [1] K. Nordlund, S. J. Zinkle, A. E. Sand, F. Granberg, R. S. Averback, R. E. Stoller, T. Suzudo,
587 L. Malerba, F. Banhart, W. J. Weber, F. Willaime, S. L. Dudarev *et al.*, *Primary radiation*
588 *damage: A review of current understanding and models*, *Journal of Nuclear Materials* **512**,
589 450 (2018), doi:<https://doi.org/10.1016/j.jnucmat.2018.10.027>.
- 590 [2] L. Volpe, T. Cebriano Ramírez, C. S. Sánchez, A. Perez, A. Curcio, D. De Luis, G. Gatti,
591 B. Kebladj, S. Khetari, S. Malko, J. A. Perez-Hernandez and M. D. R. Frias, *A platform*
592 *for ultra-fast proton probing of matter in extreme conditions*, *Sensors* **24**(16) (2024),
593 doi:[10.3390/s24165254](https://doi.org/10.3390/s24165254).
- 594 [3] S. Malko, W. Cayzac, V. Ospina-Bohórquez, K. Bhutwala, M. Bailly-Grandvaux, C. McGuffey,
595 R. Fedosejevs, X. Vaisseau, A. Tauschwitz, J. I. Apiñaniz, D. D. L. Blanco, G. Gatti *et al.*,
596 *Proton stopping measurements at low velocity in warm dense carbon*, *Nature Communica-*
597 *tions* **13**, 2893 (2022), doi:<https://doi.org/10.1038/s41467-022-30472-8>.
- 598 [4] G. Parisi, F. Romano and G. Schettino, *Microdosimetry for hadron therapy: A state of the art*
599 *of detection technology*, *Frontiers in Physics* **10** (2022), doi:[10.3389/fphy.2022.1035956](https://doi.org/10.3389/fphy.2022.1035956).
- 600 [5] Z. Huan, Y. Zheng, K. Wang, Z. Shen, W. Ni, J. Zu and Y. Shao, *Advancements in radiation*
601 *resistance and reinforcement strategies of perovskite solar cells in space applications*, *J.*
602 *Mater. Chem. A* **12**, 1910 (2024), doi:[10.1039/D3TA06388G](https://doi.org/10.1039/D3TA06388G).
- 603 [6] D. M. Fleetwood, E. X. Zhang, R. D. Schrimpf, S. T. Pantelides and S. Bonaldo, *Effects*
604 *of interface traps and hydrogen on the low-frequency noise of irradiated mos devices*, *IEEE*
605 *Transactions on Nuclear Science* **71**(4), 555 (2024), doi:[10.1109/TNS.2023.3323548](https://doi.org/10.1109/TNS.2023.3323548).
- 606 [7] K. Höflich, G. Hobler, F. I. Allen, T. Wirtz, G. Rius, L. McElwee-White, A. V. Krashenin-
607 nikov, M. Schmidt, I. Utke, N. Klingner, M. Osenberg, R. Córdoba *et al.*, *Roadmap*
608 *for focused ion beam technologies*, *Applied Physics Reviews* **10**(4), 041311 (2023),
609 doi:[10.1063/5.0162597](https://doi.org/10.1063/5.0162597).
- 610 [8] J. F. Ziegler, M. Ziegler and J. Biersack, *SRIM – the stopping and range of*
611 *ions in matter (2010)*, *Nuclear Instruments and Methods in Physics Research*
612 *Section B: Beam Interactions with Materials and Atoms* **268**(11), 1818 (2010),
613 doi:<https://doi.org/10.1016/j.nimb.2010.02.091>, 19th International Conference on Ion
614 Beam Analysis.

- 615 [9] K. Gärtner, *Ion-Solid Interaction*, pp. 3–62, Springer International Publishing, Cham,
616 ISBN 978-3-319-33561-2, doi:https://doi.org/10.1007/978-3-319-33561-2_1 (2016).
- 617 [10] W. Wesch and E. Wendler, *Ion beam modification of solids*, vol. 61, Springer,
618 doi:<https://doi.org/10.1007/978-3-319-33561-2> (2016).
- 619 [11] A. Hamedani, J. Byggmästar, F. Djurabekova, G. Alahyarizadeh, R. Ghaderi, A. Min-
620 uchehr and K. Nordlund, *Insights into the primary radiation damage of silicon by a*
621 *machine learning interatomic potential*, *Materials Research Letters* **8**(10), 364 (2020),
622 doi:[10.1080/21663831.2020.1771451](https://doi.org/10.1080/21663831.2020.1771451).
- 623 [12] N. Medvedev, A. E. Volkov, R. Rymzhanov, F. Akhmetov, S. Gorbunov, R. Voronkov and
624 P. Babaev, *Frontiers, challenges, and solutions in modeling of swift heavy ion effects in*
625 *materials*, *Journal of Applied Physics* **133**(10), 100701 (2023), doi:[10.1063/5.0128774](https://doi.org/10.1063/5.0128774).
- 626 [13] D. Roth, B. Bruckner, G. Undeutsch, V. Paneta, A. I. Mardare, C. L. McGahan, M. Dos-
627 mailov, J. I. Juaristi, M. Alducin, J. D. Pedarnig, R. F. Haglund, D. Primetzhofer *et al.*,
628 *Electronic stopping of slow protons in oxides: Scaling properties*, *Phys. Rev. Lett.* **119**,
629 163401 (2017), doi:[10.1103/PhysRevLett.119.163401](https://doi.org/10.1103/PhysRevLett.119.163401).
- 630 [14] X. Qi, F. Bruneval and I. Maliyov, *Ab initio prediction of a negative barkas coeffi-*
631 *cient for slow protons and antiprotons in lif*, *Phys. Rev. Lett.* **128**, 043401 (2022),
632 doi:[10.1103/PhysRevLett.128.043401](https://doi.org/10.1103/PhysRevLett.128.043401).
- 633 [15] A. M. Zamora-Vinaroz, P. de Vera, I. Abril and R. Garcia-Molina, *Simulation of depth-dose*
634 *curves and water equivalent ratios of energetic proton beams in cortical bone*, *Phys. Rev. E*
635 **110**, 034405 (2024), doi:[10.1103/PhysRevE.110.034405](https://doi.org/10.1103/PhysRevE.110.034405).
- 636 [16] F. Matias, T. F. Silva, N. E. Koval, J. J. N. Pereira, P. C. G. Antunes, P. T. D. Siqueira, M. H.
637 Tabacniks, H. Yoriyaz, J. M. B. Shorto and P. L. Grande, *Efficient computational modeling*
638 *of electronic stopping power of organic polymers for proton therapy optimization*, *Scientific*
639 *Reports* **14**, 9868 (2024), doi:<https://doi.org/10.1038/s41598-024-60651-0>.
- 640 [17] S. J. Blundell, R. De Renzi, T. Lancaster and F. L. Pratt, *Muon Spec-*
641 *troscopy: An Introduction*, Oxford University Press, ISBN 9780198858959,
642 doi:[10.1093/oso/9780198858959.001.0001](https://doi.org/10.1093/oso/9780198858959.001.0001) (2021).
- 643 [18] A. D. Hillier, S. J. Blundell, I. McKenzie, I. Umegaki, L. Shu, J. A. Wright, T. Prokscha,
644 F. Bert, K. Shimomura, A. Berlie, H. Alberto and I. Watanabe, *Muon spin spectroscopy*,
645 *Nature Reviews Methods Primers* **2**, 4 (2022), doi:[10.1038/s43586-021-00089-0](https://doi.org/10.1038/s43586-021-00089-0).
- 646 [19] R. Lichti, K. Chow, J. Gil, D. Stripe, R. Vilão and S. Cox, *Location of the H[+/-] level:*
647 *Experimental limits for muonium*, *Physica B: Condensed Matter* **376-377**, 587 (2006),
648 doi:<https://doi.org/10.1016/j.physb.2005.12.148>.
- 649 [20] S. F. J. Cox, J. L. Gavartin, J. S. Lord, S. P. Cottrell, J. M. Gil, H. V. Alberto, J. P. Duarte,
650 R. C. Vilão, N. A. de Campos, D. J. Keeble, E. A. Davis, M. Charlton *et al.*, *Oxide muon-*
651 *ics: II. modelling the electrical activity of hydrogen in wide-gap and high-permittivity di-*
652 *electrics*, *Journal of Physics: Condensed Matter* **18**(3), 1079 (2006), doi:[10.1088/0953-](https://doi.org/10.1088/0953-8984/18/3/022)
653 [8984/18/3/022](https://doi.org/10.1088/0953-8984/18/3/022).
- 654 [21] S. F. J. Cox, R. L. Lichti, J. S. Lord, E. A. Davis, R. C. Vilão, J. M. Gil, T. D. Veal and
655 Y. G. Celebi, *The first 25 years of semiconductor muonics at ISIS, modelling the electrical*
656 *activity of hydrogen in inorganic semiconductors and high- κ dielectrics*, *Physica Scripta*
657 **88**, 068503 (2013), doi:[10.1088/0031-8949/88/06/068503](https://doi.org/10.1088/0031-8949/88/06/068503).

- 658 [22] T. Prokscha, E. Morenzoni, K. Deiters, F. Foroughi, D. George, R. Kobler, A. Suter and
659 V. Vrankovic, *The new μ E4 beam at PSI: A hybrid-type large acceptance channel for the*
660 *generation of a high intensity surface-muon beam*, Nuclear Instruments and Methods
661 in Physics Research Section A: Accelerators, Spectrometers, Detectors and Associated
662 Equipment **595**(2), 317 (2008), doi:<https://doi.org/10.1016/j.nima.2008.07.081>.
- 663 [23] M. Hiraishi, H. Okabe, A. Koda, R. Kadono and H. Hosono, *Ambipolarity of diluted hy-*
664 *drogen in wide-gap oxides revealed by muon study*, Journal of Applied Physics **132**(10),
665 105701 (2022), doi:[10.1063/5.0102204](https://doi.org/10.1063/5.0102204).
- 666 [24] R. Kadono and H. Hosono, *Ambipolarity of hydrogen in matter revealed by muons*, Ad-
667 vances in Physics **0**(0), 1 (2024), doi:[10.1080/00018732.2024.2413342](https://doi.org/10.1080/00018732.2024.2413342).
- 668 [25] E. Fermi and E. Teller, *The capture of negative mesotrons in matter*, Phys. Rev. **72**, 399
669 (1947), doi:[10.1103/PhysRev.72.399](https://doi.org/10.1103/PhysRev.72.399).
- 670 [26] M. Senba, D. J. Arseneau, J. J. Pan and D. G. Fleming, *Slowing-down times and stop-*
671 *ping powers for ~ 2 –MeV μ^+ in low-pressure gases*, Phys. Rev. A **74**, 042708 (2006),
672 doi:[10.1103/PhysRevA.74.042708](https://doi.org/10.1103/PhysRevA.74.042708).
- 673 [27] R. C. Vilão, H. V. Alberto, R. B. L. Vieira, J. M. Gil and A. Weidinger, Reply to “Com-
674 ment on ‘Role of the transition state in muon implantation’ and ‘Thermal spike in muon
675 implantation’”, Phys. Rev. B **101**, 077202 (2020), doi:[10.1103/PhysRevB.101.077202](https://doi.org/10.1103/PhysRevB.101.077202).
- 676 [28] J. H. Brewer, V. G. Storchak, G. D. Morris and D. Eshchenko, Comment on “Role of the
677 transition state in muon implantation” and “Thermal spike in muon implantation”, Phys.
678 Rev. B **101**, 077201 (2020), doi:[10.1103/PhysRevB.101.077201](https://doi.org/10.1103/PhysRevB.101.077201).
- 679 [29] C. Kittel, *Quantum theory of solids, second edition*, page 134, John Wiley and Sons, ISBN
680 0-471-62412-8 (1987).
- 681 [30] B. D. Patterson, *Muonium states in semiconductors*, Rev. Mod. Phys. **60**, 69 (1988),
682 doi:[10.1103/RevModPhys.60.69](https://doi.org/10.1103/RevModPhys.60.69).
- 683 [31] R. C. Vilão, R. B. L. Vieira, H. V. Alberto, J. M. Gil and A. Weidinger, *Role*
684 *of the transition state in muon implantation*, Phys. Rev. B **96**, 195205 (2017),
685 doi:[10.1103/PhysRevB.96.195205](https://doi.org/10.1103/PhysRevB.96.195205).
- 686 [32] R. C. Vilão, R. B. L. Vieira, H. V. Alberto, J. M. Gil, A. Weidinger, R. L. Lichti, P. W. Mengyan,
687 B. B. Baker and J. S. Lord, *Barrier model in muon implantation and application to Lu_2O_3* ,
688 Phys. Rev. B **98**, 115201 (2018), doi:[10.1103/PhysRevB.98.115201](https://doi.org/10.1103/PhysRevB.98.115201).
- 689 [33] R. C. Vilão, H. V. Alberto, J. M. Gil and A. Weidinger, *Thermal spike in muon implantation*,
690 Phys. Rev. B **99**, 195206 (2019), doi:[10.1103/PhysRevB.99.195206](https://doi.org/10.1103/PhysRevB.99.195206).
- 691 [34] I. Lifshits, M. Kaganov and L. Tanatarov, *On the theory of radiation-induced changes*
692 *in metals*, Journal of Nuclear Energy. Part A. Reactor Science **12**(1-2), 69 (1960),
693 doi:[https://doi.org/10.1016/0368-3265\(60\)90010-4](https://doi.org/10.1016/0368-3265(60)90010-4).
- 694 [35] M. Toulemonde, C. Dufour, A. Meftah and E. Paumier, *Transient thermal processes in heavy*
695 *ion irradiation of crystalline inorganic insulators*, Nuclear Instruments and Methods in
696 Physics Research Section B: Beam Interactions with Materials and Atoms **166-167**, 903
697 (2000), doi:[https://doi.org/10.1016/S0168-583X\(99\)00799-5](https://doi.org/10.1016/S0168-583X(99)00799-5).

- 698 [36] A. Meftah, J. Costantini, N. Khalfaoui, S. Boudjadar, J. Stoquert, F. Studer and M. Toule-
699 monde, *Experimental determination of track cross-section in $gd_3ga_5o_{12}$ and comparison to*
700 *the inelastic thermal spike model applied to several materials*, Nuclear Instruments and
701 Methods in Physics Research Section B: Beam Interactions with Materials and Atoms
702 **237**(3), 563 (2005), doi:<https://doi.org/10.1016/j.nimb.2005.02.025>.
- 703 [37] R. C. Vilão, M. A. Curado, H. V. Alberto, J. M. Gil, J. A. Paixão, J. S. Lord and A. Weidinger,
704 *Paramagnetic rare-earth oxide Nd_2O_3 investigated by muon spin spectroscopy*, Phys. Rev.
705 B **100**, 205203 (2019), doi:[10.1103/PhysRevB.100.205203](https://doi.org/10.1103/PhysRevB.100.205203).
- 706 [38] R. C. Vilão, A. G. Marinopoulos, H. V. Alberto, J. M. Gil, J. S. Lord and A. Weidinger,
707 *Sapphire $\alpha - Al_2O_3$ puzzle: Joint μ SR and density functional theory study*, Phys. Rev. B
708 **103**, 125202 (2021), doi:[10.1103/PhysRevB.103.125202](https://doi.org/10.1103/PhysRevB.103.125202).
- 709 [39] A. G. Marinopoulos, R. C. Vilão, H. V. Alberto, E. F. M. Ribeiro, J. M. Gil, P. W.
710 Mengyan, M. R. Goeks, M. Kauk-Kuusik and J. S. Lord, *Hydrogen states in mixed-*
711 *cation $CuIn_{(1-x)}Ga_xSe_2$ chalcopyrite alloys: a combined study by first-principles density-*
712 *functional calculations and muon-spin spectroscopy*, Philos. Mag. **101**, 2412 (2021),
713 doi:<https://doi.org/10.1080/14786435.2021.1972178>.
- 714 [40] R. C. Vilão, H. V. Alberto, E. F. M. Ribeiro, J. M. Gil and A. Weidinger, *Muonium reaction*
715 *in semiconductors and insulators: The role of the transition state*, Journal of Physics:
716 Conference Series **2462**(1), 012056 (2023), doi:[10.1088/1742-6596/2462/1/012056](https://doi.org/10.1088/1742-6596/2462/1/012056).
- 717 [41] Y. Wan, C. Samundsett, J. Bullock, M. Hettick, T. Allen, D. Yan, J. Peng, Y. Wu,
718 J. Cui, A. Javey and A. Cuevas, *Conductive and stable magnesium oxide electron-selective*
719 *contacts for efficient silicon solar cells*, Advanced Energy Materials **7**(5), 1601863,
720 doi:<https://doi.org/10.1002/aenm.201601863>.
- 721 [42] R. da Silva Alvim, I. J. Borges and A. A. Leitão, *Proton migration on perfect, vacant, and*
722 *doped $MgO(001)$ surfaces: Role of dissociation residual groups*, The Journal of Physical
723 Chemistry C **122**(38), 21841 (2018), doi:[10.1021/acs.jpcc.8b03962](https://doi.org/10.1021/acs.jpcc.8b03962).
- 724 [43] C. Zheng, K. Zhu, S. Cardoso de Freitas, J.-Y. Chang, J. E. Davies, P. Eames, P. P. Freitas,
725 O. Kazakova, C. Kim, C.-W. Leung, S.-H. Liou, A. Ognev *et al.*, *Magnetoresistive sensor de-*
726 *velopment roadmap (non-recording applications)*, IEEE Transactions on Magnetics **55**(4),
727 1 (2019), doi:[10.1109/TMAG.2019.2896036](https://doi.org/10.1109/TMAG.2019.2896036).
- 728 [44] J. Robertson, H. Naganuma and H. Lu, *Comparing h-BN and MgO tunnel barriers for*
729 *scaled magnetic tunnel junctions*, Japanese Journal of Applied Physics **62**(SC), SC0804
730 (2023), doi:[10.35848/1347-4065/acb062](https://doi.org/10.35848/1347-4065/acb062).
- 731 [45] G. Liu, W. Chen, Z. Xiong, Y. Wang, S. Zhang and Z. Xia, *Laser-driven broadband*
732 *near-infrared light source with watt-level output*, Nature Photonics **18**(6), 562 (2024),
733 doi:<https://doi.org/10.1038/s41566-024-01400-7>.
- 734 [46] S. Wu, K.-Y. Tseng, R. Kato, T.-S. Wu, A. Large, Y.-K. Peng, W. Xiang, H. Fang, J. Mo,
735 I. Wilkinson, Y.-L. Soo, G. Held *et al.*, *Rapid interchangeable hydrogen, hydride, and proton*
736 *species at the interface of transition metal atom on oxide surface*, Journal of the American
737 Chemical Society **143**(24), 9105 (2021), doi:[10.1021/jacs.1c02859](https://doi.org/10.1021/jacs.1c02859), PMID: 34047552.
- 738 [47] B. T. Jeffries, R. Gonzalez, Y. Chen and G. P. Summers, *Luminescence in ther-*
739 *mochemically reduced MgO: The role of hydrogen*, Phys. Rev. B **25**, 2077 (1982),
740 doi:[10.1103/PhysRevB.25.2077](https://doi.org/10.1103/PhysRevB.25.2077).

- 741 [48] M. Kodu, M. Aints, T. Avarmaa, V. Denks, E. Feldbach, R. Jaaniso, M. Kirm,
742 A. Maaros and J. Raud, *Hydrogen doping of MgO thin films prepared*
743 *by pulsed laser deposition*, Applied Surface Science **257**(12), 5328 (2011),
744 doi:<https://doi.org/10.1016/j.apsusc.2010.12.006>, E-MRS 2010 Spring Meeting Sym-
745 posium R. "Laser Processing and Diagnostics for Micro and Nano Applications".
- 746 [49] H. Naganuma, *Spintronics memory using magnetic tunnel junction for X nm-generation*,
747 Japanese Journal of Applied Physics **62**(SG), SG0811 (2023), doi:[10.35848/1347-4065/accaed](https://doi.org/10.35848/1347-4065/accaed).
748
- 749 [50] R. F. Kiefl, J. B. Warren, G. M. Marshall, C. J. Oram, J. H. Brewer, D. J. Judd and L. D.
750 Spires, *Muonium and positronium production in oxide powders*, Hyperfine Interactions **6**,
751 185 (1979), doi:[10.1007/BF01028791](https://doi.org/10.1007/BF01028791).
- 752 [51] R. F. Kiefl, J. B. Warren, C. J. Oram, G. M. Marshall, J. H. Brewer, D. R. Harshman and
753 C. W. Clawson, *Surface interactions of muonium in oxide powders at low temperatures*,
754 Phys. Rev. B **26**, 2432 (1982), doi:[10.1103/PhysRevB.26.2432](https://doi.org/10.1103/PhysRevB.26.2432).
- 755 [52] D. P. Spencer, D. G. Fleming and J. H. Brewer, *Muonium formation in diamond and oxide*
756 *insulators*, Hyperfine Interactions **18**, 567 (1984), doi:[10.1007/BF02064869](https://doi.org/10.1007/BF02064869).
- 757 [53] R. F. Kiefl, W. Odermatt, H. Baumeler, J. Felber, H. Keller, W. Kündig, P. F. Meier, B. D.
758 Patterson, J. W. Schneider, K. W. Blazey, T. L. Estle and C. Schwab, *Muonium centers in*
759 *the cuprous halides*, Phys. Rev. B **34**, 1474 (1986), doi:[10.1103/PhysRevB.34.1474](https://doi.org/10.1103/PhysRevB.34.1474).
- 760 [54] W. MacFarlane, T. Parolin, D. Cortie, K. Chow, M. Hossain, R. Kiefl, C. Levy, R. McFad-
761 den, G. Morris, M. Pearson *et al.*, *$8\text{Li} + \beta\text{-nmr}$ in the cubic insulator mgo*, In *Journal*
762 *of Physics: Conference Series*, vol. 551, p. 012033. IOP Publishing, doi:[10.1088/1742-6596/551/1/012033](https://doi.org/10.1088/1742-6596/551/1/012033) (2014).
763
- 764 [55] P. Hohenberg and W. Kohn, *Inhomogeneous electron gas*, Phys. Rev. **136**, B864 (1964),
765 doi:[10.1103/PhysRev.136.B864](https://doi.org/10.1103/PhysRev.136.B864).
- 766 [56] W. Kohn and L. J. Sham, *Self-consistent equations including exchange and correlation*
767 *effects*, Phys. Rev. **140**, A1133 (1965), doi:[10.1103/PhysRev.140.A1133](https://doi.org/10.1103/PhysRev.140.A1133).
- 768 [57] R. Whited, C. J. Flaten and W. Walker, *Exciton thermoreflectance of MgO and CaO*,
769 Solid State Communications **13**(11), 1903 (1973), doi:[https://doi.org/10.1016/0038-1098\(73\)90754-0](https://doi.org/10.1016/0038-1098(73)90754-0).
770
- 771 [58] L.-P. Zhou, X.-J. Ni, Z. Salman, A. Suter, J.-Y. Tang, V. Vrankovic and
772 T. Prokscha, *Simulation studies for upgrading a high-intensity surface muon beam-*
773 *line at Paul Scherrer Institute*, Phys. Rev. Accel. Beams **25**, 051601 (2022),
774 doi:[10.1103/PhysRevAccelBeams.25.051601](https://doi.org/10.1103/PhysRevAccelBeams.25.051601).
- 775 [59] A. Stoykov, R. Scheuermann, K. Sedlak, J. Rodriguez, U. Greuter and A. Amato, *High-*
776 *Field μ SR Instrument at PSI: Detector Solutions*, Physics Procedia **30**, 7 (2012),
777 doi:<https://doi.org/10.1016/j.phpro.2012.04.028>, 12th International Conference on
778 Muon Spin Rotation, Relaxation and Resonance (μ SR2011).
- 779 [60] J. H. Van Vleck, *The dipolar broadening of magnetic resonance lines in crystals*, Phys. Rev.
780 **74**, 1168 (1948), doi:[10.1103/PhysRev.74.1168](https://doi.org/10.1103/PhysRev.74.1168).
- 781 [61] O. Hartmann, *Quadrupole influence on the dipolar-field width for a single interstitial in a*
782 *metal crystal*, Phys. Rev. Lett. **39**, 832 (1977), doi:[10.1103/PhysRevLett.39.832](https://doi.org/10.1103/PhysRevLett.39.832).

- 783 [62] μ SR experiment on the same MgO sample, at $B = 1.5$ mT and $T = 260\text{--}360$ K, performed
784 at the GPS spectrometer at the Paul Scherrer Institut.
- 785 [63] R. C. Vilão, H. V. Alberto, J. Piroto Duarte, J. M. Gil, A. Weidinger, N. Ayres de Campos,
786 R. L. Lichti, K. H. Chow and S. F. J. Cox, *Muonium spectroscopy in ZnSe: Metastability*
787 *and conversion*, Phys. Rev. B **72**, 235203 (2005), doi:[10.1103/PhysRevB.72.235203](https://doi.org/10.1103/PhysRevB.72.235203).
- 788 [64] O. Schütt, P. Pavone, W. Windl, K. Karch and D. Strauch, *Ab initio lattice dynam-*
789 *ics and charge fluctuations in alkaline-earth oxides*, Phys. Rev. B **50**, 3746 (1994),
790 doi:[10.1103/PhysRevB.50.3746](https://doi.org/10.1103/PhysRevB.50.3746).
- 791 [65] E. A. Davis, S. F. J. Cox, R. L. Lichti and C. G. Van de Walle, *Shallow donor state of hydrogen*
792 *in indium nitride*, Applied Physics Letters **82**(4), 592 (2003), doi:[10.1063/1.1539547](https://doi.org/10.1063/1.1539547),
793 https://pubs.aip.org/aip/apl/article-pdf/82/4/592/18575266/592_1_online.pdf.
- 794 [66] G. Kresse and J. Hafner, *Ab initio molecular dynamics for liquid metals*, Phys. Rev. B **47**,
795 558 (1993), doi:[10.1103/PhysRevB.47.558](https://doi.org/10.1103/PhysRevB.47.558).
- 796 [67] G. Kresse and J. Hafner, *Ab initio molecular-dynamics simulation of the liquid-metal-*
797 *amorphous-semiconductor transition in germanium*, Phys. Rev. B **49**, 14251 (1994),
798 doi:[10.1103/PhysRevB.49.14251](https://doi.org/10.1103/PhysRevB.49.14251).
- 799 [68] G. Kresse and J. Furthmüller, *Efficient iterative schemes for ab initio total-*
800 *energy calculations using a plane-wave basis set*, Phys. Rev. B **54**, 11169 (1996),
801 doi:[10.1103/PhysRevB.54.11169](https://doi.org/10.1103/PhysRevB.54.11169).
- 802 [69] J. P. Perdew, K. Burke and M. Ernzerhof, *Generalized gradient approximation made simple*,
803 Phys. Rev. Lett. **77**, 3865 (1996), doi:[10.1103/PhysRevLett.77.3865](https://doi.org/10.1103/PhysRevLett.77.3865).
- 804 [70] J. Heyd and G. E. Scuseria, *Efficient hybrid density functional calculations in solids: Assess-*
805 *ment of the Heyd-Scuseria-Ernzerhof screened Coulomb hybrid functional*, The Journal
806 of Chemical Physics **121**(3), 1187 (2004), doi:[10.1063/1.1760074](https://doi.org/10.1063/1.1760074).
- 807 [71] J. Paier, M. Marsman, K. Hummer, G. Kresse, I. C. Gerber and J. G. Ángyán, *Screened*
808 *hybrid density functionals applied to solids*, The Journal of Chemical Physics **124**(15),
809 154709 (2006), doi:[10.1063/1.2187006](https://doi.org/10.1063/1.2187006).
- 810 [72] A. G. Marinopoulos, R. C. Vilão, H. V. Alberto and J. M. Gil, *Electronic structure and mi-*
811 *gration of interstitial hydrogen in the rutile phase of TiO₂*, Journal of Physics: Condensed
812 Matter **30**(42), 425503 (2018), doi:[10.1088/1361-648X/aae0a2](https://doi.org/10.1088/1361-648X/aae0a2).
- 813 [73] N. Auerbach and V. Zelevinsky, *Doorway states in nuclear reactions as a manifes-*
814 *tation of the “super-radiant” mechanism*, Nuclear Physics A **781**(1), 67 (2007),
815 doi:<https://doi.org/10.1016/j.nuclphysa.2006.10.078>.
- 816 [74] I. Shchatsinin, H.-H. Ritze, C. P. Schulz and I. V. Hertel, *Multiphoton excitation and*
817 *ionization by elliptically polarized, intense short laser pulses: Recognizing multielec-*
818 *tron dynamics and doorway states in c₆₀ vs xe*, Phys. Rev. A **79**, 053414 (2009),
819 doi:[10.1103/PhysRevA.79.053414](https://doi.org/10.1103/PhysRevA.79.053414).
- 820 [75] V. Storchak, J. H. Brewer and G. D. Morris, *Quantum transport of electronic polarons in*
821 *sapphire*, Phys. Rev. B **56**, 55 (1997), doi:[10.1103/PhysRevB.56.55](https://doi.org/10.1103/PhysRevB.56.55).
- 822 [76] A. Suter and B. Wojek, *Musrfit: A free platform-independent framework for μ SR data anal-*
823 *ysis*, Physics Procedia **30**, 69 (2012), doi:<https://doi.org/10.1016/j.phpro.2012.04.042>,
824 12th International Conference on Muon Spin Rotation, Relaxation and Resonance
825 (μ SR2011).

- 826 [77] F. Pratt, WiMDA: a muon data analysis program for the Windows PC, *Physica*
827 *B: Condensed Matter* **289-290**, 710 (2000), doi:[https://doi.org/10.1016/S0921-](https://doi.org/10.1016/S0921-4526(00)00328-8)
828 [4526\(00\)00328-8](https://doi.org/10.1016/S0921-4526(00)00328-8).
- 829 [78] P. E. Blöchl, *Projector augmented-wave method*, *Phys. Rev. B* **50**, 17953 (1994),
830 doi:[10.1103/PhysRevB.50.17953](https://doi.org/10.1103/PhysRevB.50.17953).
- 831 [79] G. Kresse and D. Joubert, *From ultrasoft pseudopotentials to the projector augmented-wave*
832 *method*, *Phys. Rev. B* **59**, 1758 (1999), doi:[10.1103/PhysRevB.59.1758](https://doi.org/10.1103/PhysRevB.59.1758).
- 833 [80] K. Szász, T. Hornos, M. Marsman and A. Gali, *Hyperfine coupling of point defects in*
834 *semiconductors by hybrid density functional calculations: The role of core spin polarization*,
835 *Phys. Rev. B* **88**, 075202 (2013), doi:[10.1103/PhysRevB.88.075202](https://doi.org/10.1103/PhysRevB.88.075202).
- 836 [81] A. G. Marinopoulos, *Incorporation and migration of hydrogen in yttria-stabilized cubic zir-*
837 *conia: Insights from semilocal and hybrid-functional calculations*, *Phys. Rev. B* **86**, 155144
838 (2012), doi:[10.1103/PhysRevB.86.155144](https://doi.org/10.1103/PhysRevB.86.155144).
- 839 [82] C. Freysoldt, B. Grabowski, T. Hickel, J. Neugebauer, G. Kresse, A. Janotti and C. G.
840 Van de Walle, *First-principles calculations for point defects in solids*, *Reviews of modern*
841 *physics* **86**(1), 253 (2014), doi:<https://doi.org/10.1103/RevModPhys.86.253>.
- 842 [83] C. Herring, N. M. Johnson and C. G. Van de Walle, *Energy levels of isolated interstitial*
843 *hydrogen in silicon*, *Phys. Rev. B* **64**, 125209 (2001), doi:[10.1103/PhysRevB.64.125209](https://doi.org/10.1103/PhysRevB.64.125209).